ADVANCED OPTICAL MATERIALS
www.advopticalmat.de

A Terahertz Chiral Metamaterial Modulator

*Stephen J. Kindness, Nikita W. Almond, Wladislaw Michailow, Binbin Wei, Kaveh Delfanazari, Philipp Braeuninger-Weimer, Stephan Hofmann, Harvey E. Beere, David A. Ritchie, and Riccardo Degl'Innocenti**

Active control of chirality in artificial media such as metamaterials is fundamental in many scientific areas, ranging from research into fundamental optical phenomena to the investigation of novel materials, spectroscopy, and imaging. Precise control of the light polarization states has great importance for light-matter interaction in chemistry and biology, as media with diverse chiral properties react differently to the incoming polarization of light. In this work an active double layer metamaterial device based on vertically stacked ring resonators is realized by integrating electrostatically tunable graphene as an active element. The device is characterized with a THz time domain spectroscopic system demonstrating an all-electrical control of circular dichroism and optical activity at ≈2 THz, reporting a tunable ellipticity of 0.55–0.98 and >20° rotation of the plane polarization, respectively, by modifying the conductivity of graphene. Further integration with a narrow frequency quantum cascade laser emitting at ≈1.9 THz, in a crossed polarizer experimental arrangement, realizes an active amplitude modulator, hence highlighting the versatility of this approach. These results represent an important milestone for the investigation of novel concepts in optics and in several applications in the THz range, such as wireless communications and spectroscopy.

1. Introduction

Chirality is one of the principal properties in nature[1–3] and plays an important role in light matter interaction. Chiral media interact differently with right-handed circular polarized (RCP) and left-handed circular polarized (LCP) electromagnetic waves, thus showing distinctive spectroscopic and biological response. Chirality comprises two different phenomena; circular dichroism (CD) and optical activity (OA) which for application purposes are ideally considered separately while in reality are intrinsically connected and are difficult to be independently addressed. Optical activity occurs when electromagnetic waves traveling through a chiral medium experience a different real part of the refractive index depending on whether they are LCP or RCP, thus causing a rotation of the polarization plane for the transmitted light. Circular dichroism is determined by the different absorption for LCP and RCP waves in a chiral medium, thus causing a linear to elliptical polarization conversion. From the perspective of fundamental research, investigation of novel chiral media intersects fundamental intriguing concepts in modern optics, such as the engineering of negative refractive index materials,[4,5] while in technological applications it offers unique opportunities for molding the flow of light and ultimately for the development of optoelectronic devices.[6,7] Metamaterials (MMs),[8,9] subwavelength elements exhibiting artificial electromagnetic resonances, are the most suitable platform for studying chiral devices. MMs are normally engineered as metallic features over a substrate and their resonances are mainly determined by their shape and size, rather than by the choice of the materials they are composed of. Their versatility, together with their high optical confinement, which leads to strong light–matter interaction, is the key to overcome the poor chiral response of naturally occurring materials. All these features are in high demand in the terahertz (THz) frequency range, because of the lack of an efficient integrated optoelectronic platform operating in this region of the electromagnetic spectrum, which lies between photonic and electronics.[10] The realization of efficient active polarization control of THz light would help unlock a range of applications at this frequency range. THz wireless communications,[11] for instance, represent a fast-evolving field because of the saturation of the existing available spectrum and the promise of high (>100 Gbit s^{-1}) data rate transfer, which inevitably pushes wireless communications toward higher frequencies. Chiral active MMs allow the realization of external polarization and

Dr. S. J. Kindness, N. W. Almond, W. Michailow, Dr. B. Wei, Dr. H. E. Beere, Prof. D. A. Ritchie
Cavendish Laboratory
University of Cambridge
J. J. Thomson Avenue, Cambridge CB3 0HE, UK
Dr. K. Delfanazari, Dr. P. Braeuninger-Weimer, Prof. S. Hofmann
Department of Engineering
University of Cambridge
9 J. J. Thomson Avenue, Cambridge CB3 0FA, UK
Dr. R. Degl'Innocenti
Department of Engineering
University of Lancaster
Bailrigg, Lancaster LA1 4YW, UK
E-mail: r.deglinnocenti@lancaster.ac.uk
The ORCID identification number(s) for the author(s) of this article can be found under https://doi.org/10.1002/adom.202000581.

DOI: 10.1002/adom.202000581

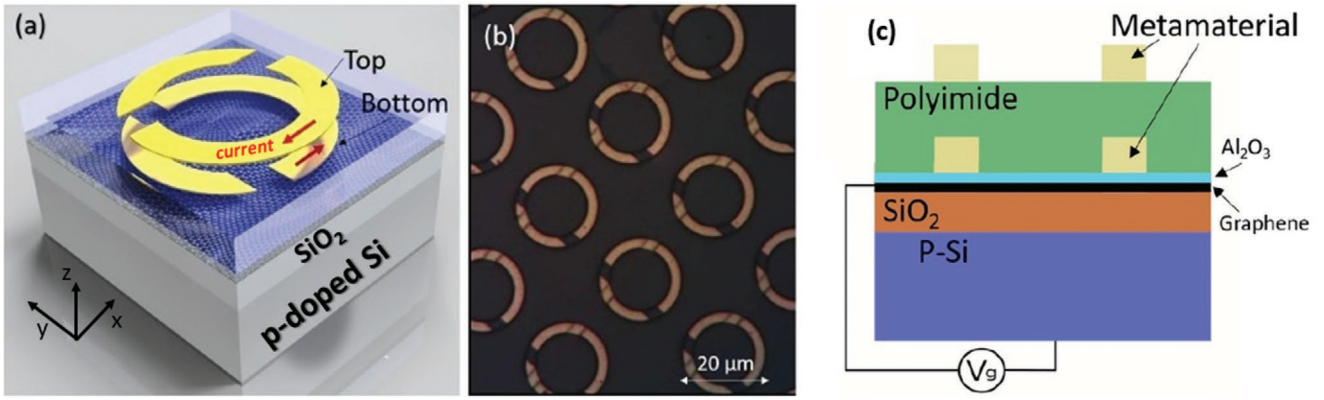

Figure 1. Chiral metamaterial unit. a) Basic schematic of a unit cell. b) Optical image of the array. c) Section of the device with the biasing configuration.

amplitude modulators to be implemented in future wireless protocols.[12] Active control of the chirality in the THz range would impact on research on topological insulators[13–15] as well and provide a fundamental tool to investigate material birefringence,[16] e.g., for pharmaceutical applications[17,18] or in stereochemistry.[19] Finally, active polarization modulators would enable the selective excitation of the rovibrational spectrum of inherently chiral biological macromolecules and complex chains, such as proteins and RNA[20] or DNA.[21] A dynamical control of THz chiral metamaterial devices has been demonstrated with different approaches, such as by using complex microelectromechanical systems[21–26] or by integrating photoactive materials such as silicon.[27–29] The former approach suffers from a limited modulation speed and from a nontrivial fabrication. The latter requires the implementation of an extra laser source, thus limiting the potential applications beyond the laboratory environment. These approaches yield large modulation depths at the expense of complex fabrication, and mostly do not provide a direct, fast electrical tuning of the polarization state polarization modulation based on VO_2 thermal modulation has been demonstrated, e.g., with broadband grating with high efficiency, but with inevitably slow reconfiguration speed.[30] The ease of integration with standard fabrication processes, and the wide carrier concentration tunability[31] via electrostatic gating, makes graphene, together with the fast (<ps) carrier momentum relaxation time,[32] the ideal active element in a THz platform. The efficiency of graphene in THz integrated devices has been reported for detectors,[33,34] amplitude,[35–38] frequency,[39–42] and polarization modulators.[43,44] A single layer graphene loaded MM active polarization device was demonstrated showing effective OA[43] and fast modulation (>5 MHz) in combination with a quantum cascade laser (QCL). Electrical tunability of chiral MMs coupled to graphene showed efficient modulation via ion-gel electrical gating.[44] In this article we report on the realization of a double layer active MM polarization device capable of achieving CD with a dynamic ellipticity modulation of ≈0.45 at 2.13 THz. Differently from other approaches based on the tunable selective absorption between RCP and LCP, such as in double layer inverse gammadions,[5,48] the chiral response here was achieved due to the interplay between dark and bright MM resonances, reminiscent of electromagnetic induced transparency. The same device also exhibits OA in excess of 20 achieving a dynamical rotation of the polarization plane >15° at 2.03 THz, remarkably with ≈0 ellipticity. This performance represents an improvement with respect to ref. [44] and was achieved with electrostatic gating instead of ion-gel. Ion-gel graphene doping is normally more effective in achieving a larger modulation depth at the expense of reconfiguration speed which is typically on the order of 10 s of kHz, well below the 10–100 MHz achievable with this approach.[37] Furthermore, this integration provides a unique fast reconfigurable tool for the active modification of the QCL polarization, which is emitted in transverse magnetic (TM) mode as dictated by the intersubband transition rules, without integrating any complex photonic patterning of the laser cavity.[45] These results pave the way to a plethora of experimental configurations where an active modulation of the THz light polarization is required.

2. Device Design and Fabrication

The architecture is based on a unit cell comprising two metallic ring resonators separated by a polyimide dielectric layer. The bottom ring is rotated by 90° with respect to the first one, as shown in **Figure 1**a. The top ring metamaterial was defined with the same procedure as the bottom one. This unit cell was used to build a mm-sized array as shown in Figure 1b to allow efficient light coupling and optical characterization. A cross-section of the device is presented in Figure 1c. The graphene conductivity is varied by electrical gating through the p-doped silicon substrate thus modifying the bottom ring resonance and the interplay with the top one, which determines the overall optical response. The device was fabricated on a 500 µm thick boron p-doped Silicon substrate with a 300 nm insulating layer of SiO_2 on top to allow electrostatic back-gating. The graphene was grown via chemical vapor deposition (CVD) on a Cu catalyst,[46,47] subsequently transferred onto the substrate, and finally patterned via optical lithography and O_2 plasma etching into 3×3 mm^2 patches. Source and drain contact pads have been realized by optical lithography followed by Ti/Au (10/100 nm) metallic evaporation. The graphene patches were then encapsulated with 100 nm of Al_2O_3 deposited via atomic layer deposition. Encapsulation of graphene[33,48] was demonstrated to be beneficial in reducing the hysteresis, protecting graphene, and finally in reducing the Dirac point to lower voltage levels when compared to exposed graphene. The bottom ring metasurface

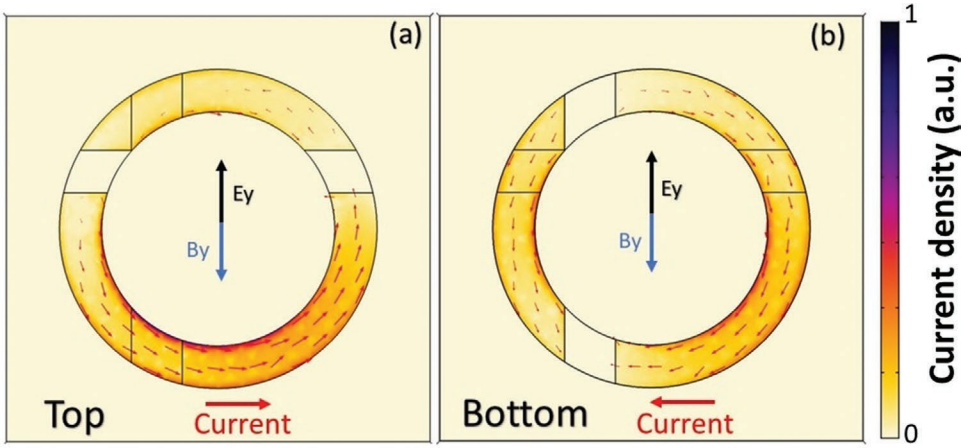

Figure 2. Simulated current excited by an incoming THz radiation incident to the sample from the top layer at resonance with E-field along the *y*-direction. a) Top layer and b) bottom layer. The two currents excited in the conjugated rings are antiparallel and give rise to a magnetic dipole and B-field component along the *y*-direction, as shown in the Supporting Information.

is fabricated through electron beam lithography, followed by Ti/Au (10/70 nm) metal evaporation and lift-off. A polyimide layer was then spun on top of the bottom metasurface, patterned as a negative photoresist leaving the bond pads uncovered before the final hard bake curing using a tube furnace. After heating the sample to 300 °C for 1 h and ramping down the temperature for a further 6 h, the hardened polyimide layer had a thickness of 1 µm. The chip was then mounted and wire-bonded on a sample holder with a 5 mm diameter hole in the back for transmission measurements.

3. Theoretical Background and Simulations

3.1. Operating Principles

Chiral materials are in general bianisotropic media where the E-field and the B-field are coupled together from Maxwell's equations through the chirality tensor.[1,2] The difference in the transmitted phase between LCP and RCP waves[1,43] yields OA, while the difference in the transmission magnitudes is related to CD and ellipticity modification. The basic operating principle of the double layer chiral MM is schematically shown in Figure 1a. The incoming THz E-field along the *y* polarization induces charges in the bottom rings which give rise to a circulating current. The top rings instead are rotated by 90° and are not directly excited by the THz radiation because of the symmetry. The current loops in the top MM rings are excited by the strong electromagnetic coupling originating from the vertical stacking. The arrangement is reminiscent of the electromagnetic induced transparency, whereas the bottom metasurface represents the bright resonator and the top metasurface the dark one. The E-field and H-field resonant modes for different graphene conductivity values are reported in the Supporting Information for completeness at different *z*-position in the unit cell. The two antiparallel currents give rise to a net magnetic dipole moment and a B-field along the y direction, as required to achieve a chiral response. This oscillating dipole moment will consequently radiate an electric field with nonzero E_x component. The modulation of the ellipticity was achieved by actively damping the bottom and top metasurfaces via graphene conductivity gating. Preliminary simulations were performed with the finite element method software COMSOL Multiphysics V5.3a, in order to investigate the optical properties of the device and to infer the optimal fabrication parameters. A single unit cell was used in these simulations having lateral Floquet boundary conditions used to simulate a continuous metamaterial array. The incoming THz radiation was simulated with a top port emitting E_y polarized plane waves toward the device structure. The Drude model was used to describe the complex conductivity of graphene and gold and the 1 µm polyimide spacer layer was described as a dielectric with a constant effective permittivity of 2.9. The details of the Drude models used can be retrieved in ref. [43]. The polymide dielectric layer is crucial to achieve a phase difference of 90° between the E_x and E_y reradiated components and in the build-up of the magnetic field, by separating the antiparallelel currents flowing in the bottom and top rings. The currents supported at resonance by the top and the bottom rings are reported in **Figure 2**a,b, respectively. Further information on the model used, e.g., on the fabrication parameters, are reported in the Supporting Information.

3.2. Finite Element Simulations

The main results for the transmitted E-field components $E_{x,y}$ are reported in **Figure 3**a–d for different graphene conductivity. The graphene conductivity range simulated is wider than the experimental measured one in order to investigate the potential of this approach, if a wider graphene conductivity range was available. As the conductivity is increased the induced currents in the resonators are dampened, leading to a lower E_x transmission and a higher E_y transmission amplitude, ultimately resulting in a reduction of the ellipticity. The frequency dependent amplitude and phase response of the transmitted E_y and E_x components are shown in Figure 3a,b. A transmission peak for $|E_x|$ and a corresponding dip for $|E_y|$ are present around 2 THz with $|E_x| > |E_y|$ at 0 mS graphene conductivity value. As

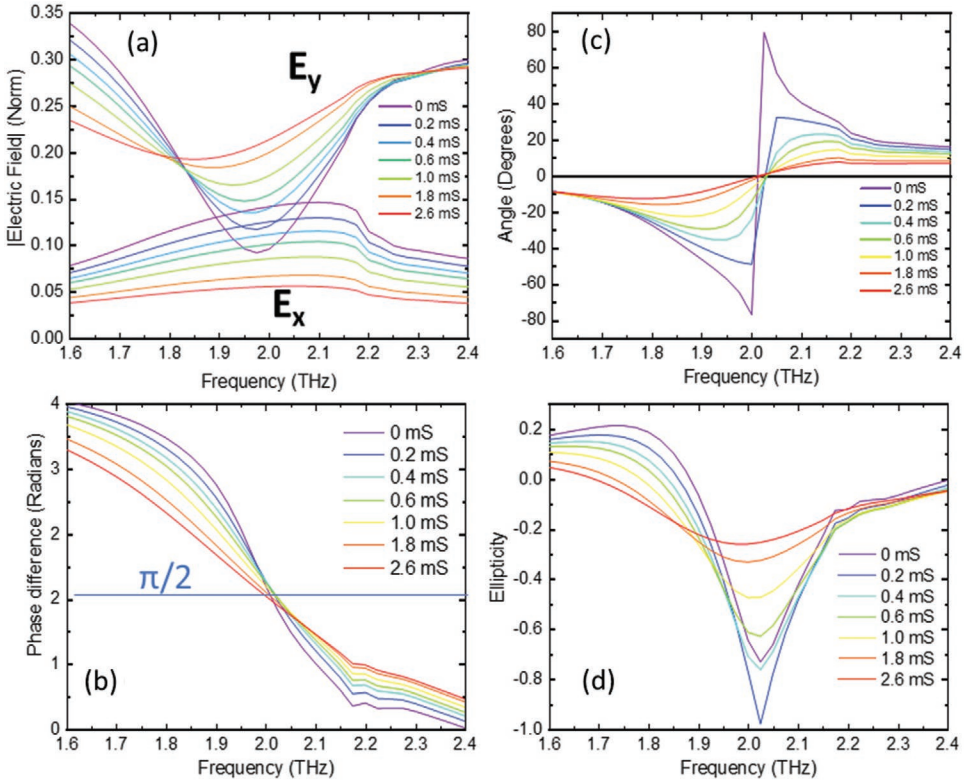

Figure 3. a) Simulated transmitted component of the E-field for an incident E_y polarized THz wave at different values of the graphene conductivity. b) The corresponding phase differences between the two E-field components. c) Rotation angle and d) ellipticity of the transmitted polarization.

the conductivity is increased to 0.2 mS, the transmission gap between $|E_x|$ and $|E_y|$ decreases until the two components have equal magnitude. Larger conductivity values yield $|E_y| > |E_x|$, as expected since the induced current is reduced and hence less power is transferred from the incoming E_y radiation to re-emitted E_x radiation. The phase difference between E_y and E_x, shown in Figure 3b, is equal to $\pi/2$ radians around 2 THz for graphene conductivity of 0 mS, yielding a similar phase difference throughout the whole conductivity range. The polarization angle and ellipticity simulations are shown in Figure 3c,d. At 2.04 THz the angle remains around 0 and the ellipticity is modulated from −1, corresponding to perfect RCP circular polarization, to −0.2, corresponding to nearly linear polarization. The same device can also be implemented as a linear polarization rotator, exploiting the OA around 1.9 THz with a dynamic angle modulation of 30° in the conductivity range between 0.2 and 2.6 mS, while keeping the ellipticity below −0.2.

4. Experimental Results

4.1. THz Time Domain Measurements

The broadband frequency response of the device was investigated by using a THz-TDS system from Menlosystems model Tera K15. In order to ensure a full polarization control, the THz spectrometer setup was modified following a procedure reported in ref. [43]. Two metal grid polarizers were inserted in the optical path to allow the correct retrieval of the transmitted E-field components by taking into account the eventual cross-talk between the polarized incoming E-field and the detector. A preliminary mandatory step involved the determination of the graphene conductivity range accessible. The current flowing between source and drain (grounded) contacts was retrieved at different back-gate voltages by applying a constant voltage of few mV, with the help of two Keithley source/measurements units. The conductivity was inferred from these measurements taking the geometrical size of the graphene patches into account. The results are reported in **Figure 4**a. The graphene was encapsulated with Al_2O_3 to prevent the Dirac point from drifting with time due to exposure to contaminants in the air, or from the polyimide processing. This was beneficial in reducing the hysteresis and bringing the Dirac point to lower voltages.[48] The graphene achievable conductivity ranged from 0.4 mS at ≈+35 V to ≈0.9 mS at ±100 V. The mobility for the holes and electrons was different, leading to an asymmetrical Dirac curve. The Dirac point was found to be at −30 V, which is consistent with n-doping, in contrast with the p-doped behavior often observed in exposed CVD grown graphene. This effect was attributed to the Al_2O_3 graphene encapsulation. The double layer device was placed in the polarization sensitive TDS setup described in ref. [43] to determine the transmitted E_y and E_x components when E_y is incident. A time domain exemplar graph for the $E_x(t)$ waveforms acquired at −35 V (≈Dirac point, black trace) and +100 V back gate voltage (red trace) is shown in Figure 4b. Similar measurements were acquired for the $E_y(t)$ component as well. The experimental measurements presented in **Figure 5**a,b are in excellent agreement with the theoretical

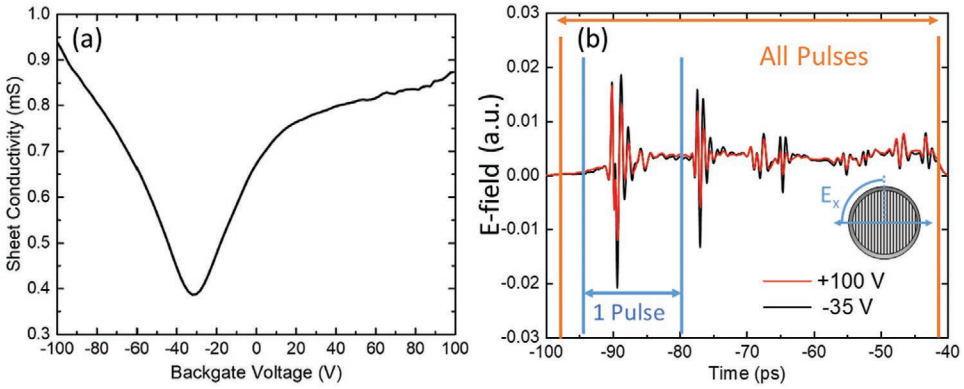

Figure 4. a) Graphene sheet conductivity. b) Typical THz-TDS time waveform acquired with crossed polarizers in order to retrieve the E_x component of the transmitted E-field.

curves shown in Figure 3a,b. The multipeaks waveform is composed of different pulses separated in time due to internal reflections at the sample/air interfaces. The first pulse through the sample was selected by applying a 15 ps Cosine window. A Fourier transform was performed to determine the frequency dependent components of $E_{x,y}$. The determination of the final values for $E_x(f)$ and $E_y(f)$ required the previously acquired correction introduced by the crosstalk between the two polarizations. The corrected values for the amplitude and phase of E_x and E_y are shown in Figure 5a,b. The measured transmitted $|E_y|$ and $|E_x|$ components, presented in Figure 5a, show a peak in $|E_x|$ and a corresponding dip in $|E_y|$ at around 2.15 THz. The ratio between these values, $|E_y|/|E_x|$, which would ideally be 1 for perfect circular polarization, is tuned from 1.2 to 2.2 as the backgate voltage is swept from −35 to +100 V. The corresponding ratio obtained from the simulations and shown in Figure 3a around 2.04 THz is 1.2 and 2.5 for graphene conductivities of 0.4 and 1.0 mS, respectively, in very good agreement with the experimental results. By comparing the TDS results with the numerical simulation values in Figure 4, there is a notable 100 GHz blue shift at 2 THz for the TDS measured value, which is consistent with the difference between real and simulated values for previously measured devices. This discrepancy could be attributed to the difference between the simulated plane wave incident THz radiation and the Gaussian shaped transmitted pulses. Figure 5b reports the measured phase difference between E_y and E_x. The device at 2.15 THz exhibited a phase difference of $\pi/2$ from the Dirac point to the highest backgate voltage of +100 V, with minimal frequency shift, in very good agreement with the trend predicted in Figure 3b. The transmitted linearly polarized E-field components can be converted into T_{RCP} and T_{LCP} radiation using the Jones formalism.[49] Accordingly, the ellipticity ε, defined as in ref. [28] and the polarization angle θ as a function of frequency[1] are determined using Equations (1) and (2) respectively

$$\varepsilon = \frac{|T_{RCP}| - |T_{LCP}|}{|T_{RCP}| + |T_{LCP}|} \tag{1}$$

$$\theta = \frac{1}{2}\left(\arg\left(T_{LCP}\right) - \arg\left(T_{RCP}\right)\right) \tag{2}$$

The ellipticity, defined as the ratio of the semi-minor to semi-major axes of the polarization ellipse, quantifies the CD while the polarization rotation angle reports the change in OA. The corresponding resulting values are reported in **Figure 6**a,b, respectively. The ellipticity of the transmitted radiation at 2.15 THz is modulated from −0.47 to −0.78 as the backgate voltage is increased from −35 to +100 V while the angle is rotated from 0°

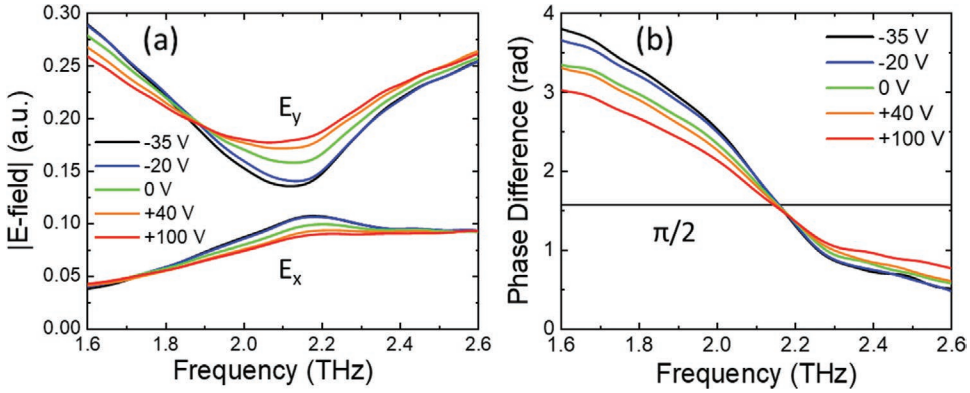

Figure 5. a) TDS measurement of $|E_y|$ and $|E_x|$ components transmitted through double layer device for different backgate voltages. b) Corresponding phase difference between E_y and E_x.

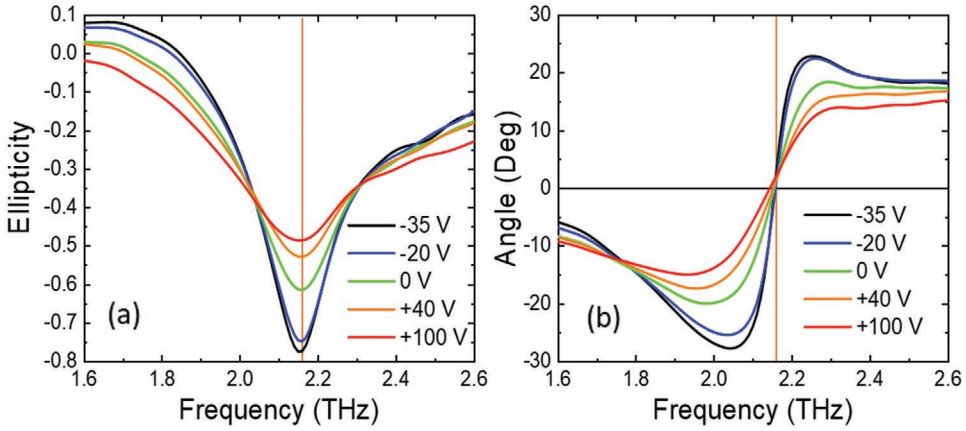

Figure 6. a) Transmitted ellipticity and b) polarization angle rotation at different backgate voltages.

to −10°. The ellipticity modulation recorded is currently limited by the graphene conductivity range achievable in this device. However, this approach is compatible with larger conductivity ranges, e.g., from 0.3 to 1.3 mS as already reported.[43]

4.2. Integration with Quantum Cascade Lasers

The THz–TDS setup allowed the temporal separation of multiple pulses and a characterization of the chiral properties of the MM/graphene device. However, the implementation of the polarization modulator with narrow-linewidth sources, such as QCLs, necessarily requires taking into account multiple reflections arising from the Fabry Perot effect. This task was accomplished by considering all the pulses acquired in Figure 4b and by repeating the same procedure for the retrieval of $E_y(f)$ and $E_x(f)$ at different backgate voltages already discussed in THz time domain measurements section. The Fourier transformation of the whole $E_{x,y}$ waveforms, taking into account the multiple internal reflections in the device resulted in a new tuning range of $|E_y|/|E_x|$ from 1 to 1.9 as the voltage was swept from −35 to +100 V. At the Dirac point, $|E_y|/|E_x|$ is ≈1, resulting in a nearly perfectly circular polarization. A similar effect was observed on the measured phases while E_x was consistently shifted by $\pi/2$ around 2.15 THz. Polar plots determined by using Equations (1) and (2) considering only the first transmitted pulse and then all the pulses are reported in **Figure 7**a,b, respectively. The frequency of the maximum change in ellipticity was achieved at 2.15 THz for the first pulse and shifted to 2.13 THz when considering the entire time waveform. The improved ellipticity tuning range spanned from −0.55 to −0.98, demonstrating almost perfect circular polarization at the Dirac point. The rotation angle increased but since the ellipticity was close to 1, it had a minor effect. The device was then integrated with a quantum cascade laser source. For maximum modulation of the ellipticity, ideally a single mode laser emitting at 2.13 THz should be used. However, due to the lack of available lasers emitting in a single mode at that frequency, a 1.94 THz QCL was used instead. The light–current–voltage characteristics of the device as well as its spectrum are reported in the Supporting Information. The chiral polarization modulator is suitable to be implemented for an all-electronic control

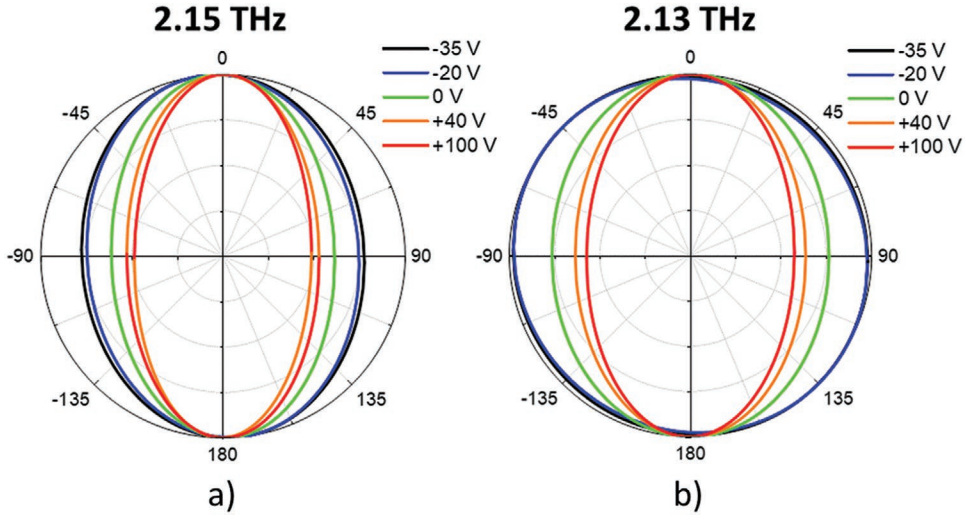

Figure 7. Polar plot for the chiral device obtained by considering a) only the first transmitted pulses and b) the full time waveforms.

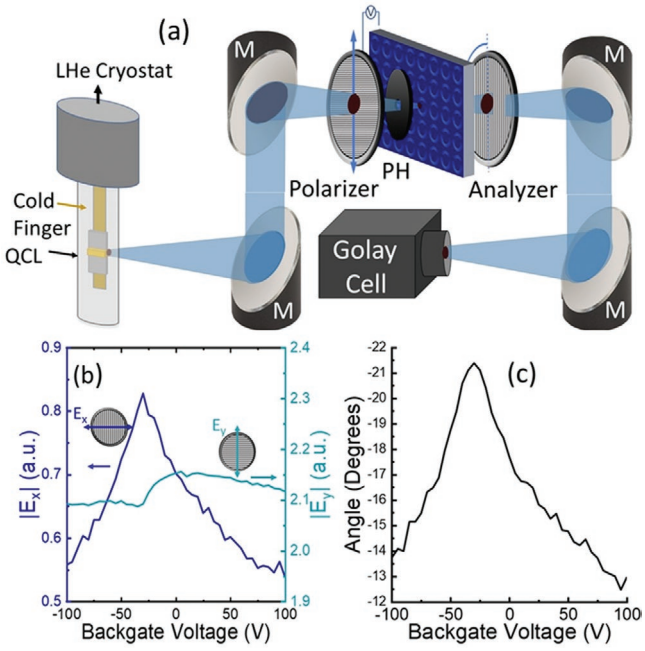

Figure 8. a) Schematic of the QCL polarization sensitive setup: M: parabolic mirror; PH: pin–hole. b) Recorded E-field components as a function of the back gate voltage. c) Recorded rotation of the polarization plane for the QCL radiation emitted at 1.94 THz as a function of the back gate voltages.

of OA around 1.9 THz while keeping the ellipticity near 0.1. The QCL is based on a bound-to-continuum design and processed into a 3 mm long single plasmon waveguide. The chiral device was inserted into a polarization sensitive experimental setup comprising QCL source, polarizer and analyzer metallic grids and Golay cell as detector, as shown in **Figure 8**a. By carefully acting on the grid polarizers, the values of $|E_y|$ and $|E_x|$ were acquired as a function of the backgate voltages. The measurements, after having been corrected for the crosstalk, are reported in Figure 8b. The QCL emitted polarized radiation is TM as dictated by the intersubband selection rules of the active region. Because of the experimental positioning of the cryostat, the E-field was emitted in the y-direction. The measured ellipticity was around 0.1 at 1.94 THz, consistently with the ellipticity retrieved by the TDS measurements and shown in Figure 7b. The $|E_y|$ values measured and reported in Figure 8b remained relatively unchanged by sweeping the backgate voltage, as expected. Conversely, the $|E_x|$ component was modulated between 0.825 and 0.55, corresponding to a 33% modulation amplitude tuning range and to 56% in transmission power. As shown in Figure 8c the tuning range accessible for the polarization angle was between −12.5° and −21.5° as the backgate voltage was swept, again in very good agreement with the graphene conductivity trend shown in Figure 4a and consistent with the TDS measurements, which yielded an OA from −18° to −28° at 1.94 THz. The minor discrepancies recorded were attributed to the nonperfect QCL alignment with respect to the sample, which translated into power leaking around the active area, causing a reduction in the polarization rotation.

5. Conclusion

A terahertz chiral device has been demonstrated based on a double layer metamaterial architecture with integrated graphene monolayer. By electrostatically tuning the graphene conductivity the optical response of the device due to the interplay between the two metasurfaces was modulated presenting tunable optical activity or circular dichroism depending on the frequency range targeted. The chiral design was simulated with the finite element software Comsol Multiphysics and a thorough experimental characterization has been performed with a THz-time domain spectroscopic (TDS) polarization sensitive setup, yielding remarkable agreement with the theoretical predictions. By changing the graphene conductivity between 0.4 and 0.9 mS, the ellipticity was modulated from 0.55 to ≈1 at 2.13 THz, thus effectively converting incident linear polarized radiation to circular polarization. A maximal continuous tuning of the optical activity of ≈20° was recorded around 2.1 THz. The device was efficiently coupled with a single plasmon QCL emitting at 1.94 THz. The optical activity of the chiral modulator has been exploited in combination with this laser in a classical crossed polarizer scheme, yielding ≈10° rotation while maintaining the ellipticity below 0.1. This configuration realized an integrated, fast amplitude modulator with modulation depth >50%. These results address fundamental concepts in optics, such as chirality, stereo-metamaterials, while providing a compact, versatile, and efficient device capable of impacting a vast range of applications in THz polarization spectroscopy, imaging, and novel materials characterization.

Supporting Information

Supporting Information is available from the Wiley Online Library or from the author.

Acknowledgements

S.J.K. acknowledges the Integrated Photonic and Electronic Systems Centre for Doctoral Training (Grant No. EP/L015455/1) for funding and support. S.J.K., N.W.A., B.W., W.M., H.E.B., and D.A.R. acknowledge financial support from the Engineering and Physical Sciences Research Council (EPSRC, Grant No. EP/P021859/1, Hyper Terahertz). W.M. thanks the George and Lillian Schiff Foundation of the University of Cambridge for financial support and is grateful for the Honorary Vice-Chancellor's Award of the Cambridge Trust. R.D. acknowledges support from the EPSRC (Grant No. EP/S019383/1) and from the Royal Society (RSG/R1/180148 – Research Grant). S.H. and P.B.-W. acknowledge funding from the EPSRC (Grant No. EP/K016636/1). P.B.-W. acknowledges the EPSRC Cambridge NanoDTC (Grant No. EP/G037221/1).

Data Availability

The datasets that support the findings of this study are openly available from Lancaster University's repository PURE at https://doi.org/10.17635/lancaster/researchdata/363.

Conflict of Interest

The authors declare no conflict of interest.

Keywords

chirality, graphene, metamaterials, quantum cascade lasers, terahertz modulators

Received: April 5, 2020
Revised: July 30, 2020
Published online: August 16, 2020

[1] Z. Wang, F. Cheng, T. Winsor, Y. Liu, *Nanotechnology* **2016**, *27*, 412001.
[2] S. S. Oh, O. Hess, *Nano Convergence* **2015**, *2*, 24.
[3] S. Bordács, I. Kézsmárki, D. Szaller, L. Demkó, N. Kida, H. Murakawa, Y. Onose, R. Shimano, T. Rõõm, U. Nagel, S. Miyahara, N. Furukawa, Y. Tokura, *Nat. Phys.* **2012**, *8*, 734.
[4] J. B. Pendry, *Science* **2004**, *306*, 1353.
[5] J. Zhou, J. Dong, T. Koschny, M. Kafesaki, C. M. Soukoulis, *Phys. Rev. B* **2009**, *79*, 121104(R).
[6] M. Rahm, J. S. Li, W. J. Padilla, *J. Infrared, Millimeter, Terahertz Waves* **2013**, *34*, 1.
[7] R. Degl'Innocenti, S. J. Kindness, H. E. Beere, D. A. Ritchie, *Nanophotonics* **2018**, *7*, 127.
[8] W. Withayachumnankul, D. Abbott, *IEEE Photonics J.* **2009**, *1*, 99.
[9] H. T. Chen, A. J. Taylor, N. Yu, *Rep. Prog. Phys.* **2016**, *79*, 076401.
[10] M. Tonouchi, *Nat. Photonics* **2007**, *1*, 97.
[11] T. Nagatsuma, G. Ducournau, C. C. Renaud, *Nat. Photonics* **2016**, *10*, 371.
[12] N. Oshima, K. Hashimoto, S. Suzuki, M. Asada, *IEEE Trans. Terahertz Sci. Technol.* **2017**, *7*, 593.
[13] G. S. Jenkins, A. B. Sushkov, D. C. Schmadel, N. P. Butch, P. Syers, J. Paglione, H. D. Drew, *Phys. Rev. B* **2010**, *82*, 125120.
[14] H. Plank, S. D. Ganichev, *Solid-State Electron.* **2018**, *147*, 44.
[15] J. W. McIver, D. Hsieh, H. Steinberg, P. Jarillo-Herrero, N. Gedik, *Nat. Nanotechnol.* **2012**, *7*, 96.
[16] L. Zhang, H. Zhong, C. Deng, C. Zhang, Y. Zhao, *Opt. Express* **2010**, *18*, 20491.
[17] D. Markl, A. Strobel, R. Schlossnikl, J. Bøtker, P. Bawuah, C. Ridgway, J. Rantanen, T. Rades, P. Gane, K.-E. Peiponen, J. A. Zeitler, *Int. J. Pharm.* **2018**, *538*, 188.
[18] A. J. Hutt, S. C. Tan, *Drugs* **1996**, *52*, 1.
[19] Y. Zhao, A. N. Askarpour, L. Sun, J. Shi, X. Li, A. Alù, *Nat. Commun.* **2017**, *8*, 14180.
[20] B. M. Fischer, M. Hoffmann, H. Helm, R. Wilk, F. Rutz, T. Kleine-Ostmann, M. Koch, P. U. Jepsen, *Opt. Express* **2005**, *13*, 5205.
[21] J. Xu, G. Ramian, J. Galan, *Astrobiology* **2003**, *3*, 489.
[22] P. Pitchappa, C. P. Ho, L. Cong, R. Singh, N. Singh, C. Lee, *Adv. Opt. Mater.* **2016**, *4*, 391.
[23] L. Cong, P. Pitchappa, N. Wang, R. Singh, *Research* **2019**, *2019*, 7084251.
[24] T. Kan, A. Isozaki, N. Kanda, N. Nemoto, K. Konishi, K. H. Takahashi, M. Kuwata-Gonokami, K. Matsumoto, I. Shimoyama, *Nat. Commun.* **2015**, *6*, 8422.
[25] P. Liu, Z. Liang, Z. Lin, Z. Xu, R. Xu, D. Yao, Y.-S. Lin, *Sci. Rep.* **2019**, *9*, 9917.
[26] M. Manjappa, P. Pitchappa, N. Singh, N. Wang, N. I. Zheludev, C. Lee, R. Singh, *Nat. Commun.* **2018**, *9*, 4056.
[27] S. Zhang, J. Zhou, Y. S. Park, J. Rho, R. Singh, S. Nam, A. K. Azad, H. T. Chen, X. Yin, A. J. Taylor, X. Zhang, *Nat. Commun.* **2012**, *3*, 942.
[28] J. Zhou, D. R. Chowdhury, R. Zhao, A. K. Azad, H. T. Chen, C. M. Soukoulis, A. J. Taylor, J. F. O'Hara, *Phys. Rev. B* **2012**, *86*, 035448.
[29] L. Cong, Y. K. Srivastava, H. Zhang, X. Zhang, J. Han, R. Singh, *Light: Sci. Appl.* **2018**, *7*, 28.
[30] X. Liu, X. Chen, E. P. J. Parrott, C. Han, G. Humbert, A. Crunteanu, E. Pickwell-MacPherson, *APL Photonics* **2018**, *3*, 051604.
[31] D. K. Efotov, P. Kim, *Phys. Rev. Lett.* **2010**, *105*, 256806.
[32] B. Sensale-Rodríguez, R. Yan, L. Liu, D. Jena, H. G. Xing, *Proc. IEEE* **2013**, *101*, 1705.
[33] R. Degl'Innocenti, L. Xiao, S. J. Kindness, V. S. Kamboj, B. Wei, P. Braeuninger-Weimer, K. Nakanishi, A. I. Aria, S. Hofmann, H. E. Beere, D. A. Ritchie, *J. Phys. D: Appl. Phys.* **2017**, *50*, 174001.
[34] R. Degl'Innocenti, L. Xiao, D. S. Jessop, S. J. Kindness, Y. Ren, H. Lin, J. A. Zeitler, J. A. Alexander-Webber, H. J. Joyce, P. Braeuninger-Weimer, S. Hofmann, H. E. Beere, D. A. Ritchie, *ACS Photonics* **2016**, *3*, 1747.
[35] R. Degl'Innocenti, D. S. Jessop, C. W. O. Sol, L. Xiao, S. J. Kindness, H. Lin, J. A. Zeitler, P. Braeuninger-Weimer, S. Hofmann, Y. Ren, V. S. Kamboj, J. P. Griffiths, H. E. Beere, D. A. Ritchie, *ACS Photonics* **2016**, *3*, 464.
[36] S. J. Kindness, D. S. Jessop, B. Wei, R. Wallis, V. S. Kamboj, L. Xiao, Y. Ren, P. Braeuninger-Weimer, A. I. Aria, S. Hofmann, H. E. Beere, D. A. Ritchie, R. Degl'Innocenti, *Sci. Rep.* **2017**, *7*, 7657.
[37] D. S. Jessop, S. J. Kindness, L. Xiao, P. Braeuninger-Weimer, H. Lin, Y. Ren, C. X. Ren, S. Hofmann, J. A. Zeitler, H. E. Beere, D. A. Ritchie, R. Degl'Innocenti, *Appl. Phys. Lett.* **2016**, *108*, 171101.
[38] Y. Sun, R. Degl'Innocenti, D. A. Ritchie, H. E. Beere, L. Xiao, M. Ruggiero, J. A. Zeitler, R. I. Stantchev, D. Chen, Z. Peng, E. MacPherson, X. Liu, *Photonics Res.* **2018**, *6*, 1151.
[39] P. Q. Liu, I. J. Luxmoore, S. A. Mikhailov, N. A. Savostianova, F. Valmorra, J. Faist, G. R. Nash, *Nat. Commun.* **2015**, *6*, 8969.
[40] S. J. Kindness, N. W. Almond, B. Wei, R. Wallis, W. Michailow, V. S. Kamboj, P. Braeuninger-Weimer, S. Hofmann, H. E. Beere, D. A. Ritchie, R. Degl'Innocenti, *Adv. Opt. Mater.* **2018**, *6*, 1800570.
[41] H. Jung, H. Jo, W. Lee, B. Kim, H. Choi, M. S. Kang, H. Lee, *Adv. Opt. Mater.* **2019**, *7*, 1801205.
[42] M. M. Jadidi, A. B. Sushkov, R. L. Myers-Ward, A. K. Boyd, K. M. Daniels, D. Kurt Gaskill, M. S. Fuhrer, H. D. Drew, T. E. Murphy, *Nano Lett.* **2015**, *15*, 7099.
[43] S. J. Kindness, N. W. Almond, W. Michailow, B. Wei, L. A. Jakob, K. Delfanazari, P. Braeuninger-Weimer, S. Hofmann, H. E. Beere, D. A. Ritchie, R. Degl'Innocenti, *ACS Photonics* **2019**, *6*, 1547.
[44] T.-T. Kim, S. S. Oh, H.-D. Kim, H. S. Park, O. Hess, B. Min, S. Zhang, *Sci. Adv.* **2017**, *3*, e1701377.
[45] G. Liang, Y. Zeng, X. Hu, H. Yu, H. Liang, Y. Zhang, L. Li, A. G. Davies, E. H. Linfield, Q. J. Wang, *ACS Photonics* **2017**, *4*, 517.
[46] S. Hofmann, P. Braeuninger-Weimer, R. S. Weatherup, *J. Phys. Chem. Lett.* **2015**, *6*, 2714.
[47] P. Braeuninger-Weimer, B. Brennan, A. J. Pollard, S. Hofmann, *Chem. Mater.* **2016**, *28*, 8905.
[48] J. A. Alexander-Webber, A. A. Sagade, A. I. Aria, Z. A. Van Veldhoven, P. Braeuninger-Weimer, R. Wang, A. Cabrero-Vilatela, M.-B. Martin, J. Sui, M. R. Connolly, S. Hofmann, *2D Mater.* **2016**, *4*, 011008.
[49] H.-A. Bachor, T. C. Ralph, *A Guide to Experiments in Quantum Optics*, 2nd ed., Wiley-VCH, Weinheim, Germany **2004**.